Topological protection breakdown: A route to frustrated ferroelectricity

(Received 6 February 2025; accepted 1 August 2025; published 10 October 2025)

Phases manifesting topological patterns in functional systems, like ferroelectric and ferromagnetic vortex superlattices, can manifest intricate and apparently ungovernable behavior, typical of frustrated nonergodic states with high-dimensional energy landscapes. This is also the case for potassium-tantalate-niobate (KTN) crystals. These transparent ferroelectrics manifest remarkable but little understood metastable domain patterns at optical (micrometer and above) scales near the cubic-to-tetragonal structural phase transition. Here, we formulate the topological breakdown model based on the competition between intrinsic scales of domain-domain collinear and noncollinear interactions associated with polarization-charge screening. The model is able to explain observed KTN mesoscopic domain patterns and phase diagram as a function of temperature and external electric field. Findings include a precise set of sharp and broad percolative transitions that are experimentally verified, validating our model. Our study identifies the central role played by competing topologically protected states, identifying a fundamental link between topological protection and frustration that supports a hitherto unexplored functional nonergodic arena.

DOI: 10.1103/h6j7-cgwz

Disordered ferroelectric crystals can manifest history dependence and frustrated behavior in proximity of their structural phase transitions, features that affect response to various degrees, becoming dominant in so-called relaxor ferroelectrics [1-6]. The regime forms a modeling challenge, as conventional frustration mechanisms, including Griffiths phases and glassy states, fail to fully account for key experimental features [3,7]. In a subset of disordered ferroelectrics, including solid solution of potassium-tantalateniobate (KTN), the complex relaxorlike behavior [3,5] coincides with the emergence of domain ordering in the form of ferroelectric superlattices or supercrystals [8]. These patterns appear connected to built-in striations [9,10] or engineered heterostructures [11,12], coupled to the reduction of volume polarization charge $\nabla \cdot \mathbf{p} \simeq 0$, where \mathbf{p} is the spontaneous polarization field. The constraint introduces closed-loop or flux-closure conditions, so that energetically preferred structures appear in the form of ferroelectric topological defects [13,14]. These have topological protection, in that each domain in the pattern can be reoriented only at the expense of modifying all the others [15]. The

Published by the American Physical Society under the terms of the Creative Commons Attribution 4.0 International license. Further distribution of this work must maintain attribution to the author(s) and the published article's title, journal citation, and DOI.

question naturally arises if there is a connection between these topological features and the emergence of complexity-driven frustrated behavior. In fact, the volume-charge screening condition makes **p** topologically analogous to a magnetic induction field, suggesting that domain-domain interaction can also be governed, at the mesoscale, by effective interaction terms that are typical of magnetic interaction. At present, no effective domain interaction model has been proposed to take into account both standard collinear dipole-dipole interaction and effective magneticlike noncollinear interaction, leaving the connection between closed-flux topologically protected domain patterns and frustration largely unexplored.

We here formulate the topological breakdown model (TBM) with the aim of identifying the role of effective noncollinear interaction in determining complex mesoscopic (from several micrometers to hundreds of micrometers) domain pattern behavior in systems supporting ferroelectric superlattices. The model is based on the competition between intrinsic mesoscopic scales through both collinear and noncollinear interactions that emerge geometrically from discrete-inversion-symmetry-breaking and volume-chargescreening flux-closure constraints [16,17]. Computational analysis and real-space renormalization group techniques allow us to describe how ensembles of flux-closure patterns and superlattices react to external stimuli. Predictions of the domain pattern phase diagram versus temperature and versus electric bias field identify a frustrated metastable phase that is experimentally confirmed in near-transition KTN:Li using percolation analyses. Our findings link directly topologically

^{*}Contact author: pablo.villegas@cref.it

protected defects to frustration and expand our ability to design and control ferroelectric response.

I. THE TOPOLOGICAL PROTECTION BREAKDOWN MODEL FOR FERROELECTRICS

We develop the TBM starting from the basic fact that the elementary cell of ordinary ferroelectric perovskites (ABO₃) above T_C exhibits a cubic symmetry. In the vicinity of T_C , the B ion features an atomic displacement along the fourfold axis, leading to a discrete-inversion-symmetry breaking, which induces a distorted electron distribution and spontaneous electric polarization [18]. We note that this picture holds for many disordered perovskite ferroelectrics, such as KTN [19], but may not apply to the class of relaxor ferroelectrics, such as PMN, where well-defined structural transitions are not observed [20,21]. Phenomenologically, below T_C , a finite sample relaxes into a pattern of different ferroelectric domains, mesoscopic regions in which the polarization is parallel to a given crystal axis. While each domain enucleates independently with a specific macroscopic polarization p, as these grow, regions with different spontaneous polarization meet, fusing together or forming topological defects in the form of domain walls. Based on Maxwell's electrostatic equations, domains arrange to allow the screening of volume polarization charge, i.e., the minimization of $\nabla \cdot \mathbf{p}$ [22]. This leads to two types of defects [see Fig. 1(a)]: type (i) walls that separate two domains with antiparallel polarization with $\mathbf{p}_i = -\mathbf{p}_i$ and type (ii) walls that form between orthogonal polarizations $\mathbf{p}_i \cdot \mathbf{p}_i = 0$. For a given starting close-packed multidomain distribution, dynamics appear driven by domain dipole-dipole interaction with the constraint that $\nabla \cdot \mathbf{p} \simeq 0$ on the walls. While dipole-dipole-like interaction, dominant across type (i) defects, can be described through the paradigmatic Heisenberg model ($\mathcal{H}_H \propto J_{ij} \mathbf{p}_i \cdot \mathbf{p}_j$), the interaction across type (ii) walls is governed by polarization-charge screening, i.e., by noncollinear interactions.

Peculiar phenomena involving noncollinear interaction have been discussed in magnetic systems in the form of magnetic topological defects [23], spin-orbit torques [24], or magnetically driven ferroelectricity [25], and are associated with spin-orbit coupling [26]. In these, the so-called Dzyaloshinskii-Moriya interaction (DMI) [27,28] underlies many chiral topological magnetic structures, such as skyrmions, and leads to a strong impact on spin dynamics [29]. However, its electric counterpart has rarely been considered. Still, recent first-principles simulations of perovskites [30] have demonstrated that electric DMI might originate from the existence of oxygen octahedral tiltings in combination with symmetry arguments [30]. This amounts to the counterpart of the magnetic spin-current model [31]. Recent experimental results have shown DMI-induced polar vortices in single thin ferroelectric films [32]. In turn, DMI is rather weak in many material systems and is typically accompanied by a much stronger Heisenberg exchange coupling. The empirical relevance of DMI to relaxor ferroelectrics is far from established. We model noncollinear interactions by introducing an energetic term $\mathcal{H}_D \propto \mathbf{D}_{ij} \cdot (\mathbf{p}_i \times \mathbf{p}_j)$, which is analogous to the DMI encountered in ferromagnetic systems [29]. As recently discussed for ferroelectrics [30], this type

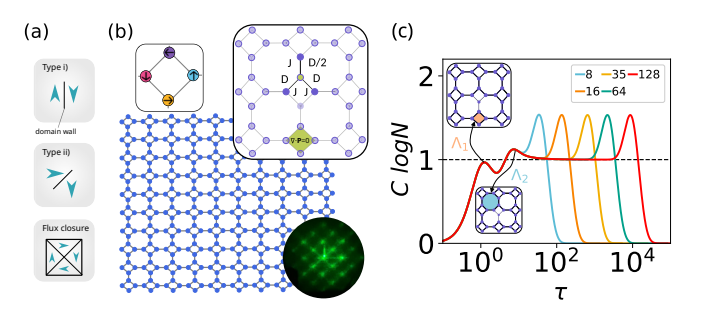


FIG. 1. (a) Different types of defects: type (i) and type (ii), and a flux-closure cell. (b) SC-tiling lattice and sketch of the energetic constants. We highlight the anisotropy in the Dzyaloshinskii-Moriya interaction. The upper left insets show a microscopic vortex, and the lower inset is an experimental far-field imaging of an SC state (right, see below). (c) Specific heat (C) vs the temporal resolution parameter τ of 2D SC lattices of different sides L (see legend, $N=4L^2$). Insets show the two possible ultraviolet cutoffs, Λ_1 and Λ_2 , the smallest scales showing translational invariance. The black dashed line highlights the plateau at C=1.

of interaction can arise from specific microscopic mechanisms, such as oxygen octahedral tiltings or anisotropy at mesoscopic scales [30,33]. In the TBM, it arises from the charge-screening constraint. The term "breakdown" refers here specifically to the loss of topological protection associated with flux-closure configurations. These configurations, stabilized by the local constraint $\nabla \cdot \mathbf{p} = 0$, are dynamically robust and can only be destroyed via coordinated, nonlocal domain rearrangements, thus functionally mimicking topological defects in low-dimensional systems. The breakdown occurs when thermal fluctuations or applied external fields induce a transition from vortex-protected states to states with extended or reoriented domains, inducing the collapse of this protection mechanism.

The Hamiltonian can be thus written as $\mathcal{H} = \mathcal{H}_H + \mathcal{H}_D + \mathcal{H}_e$, with \mathcal{H}_H representing the Heisenberg interaction, \mathcal{H}_D the DMI interaction, and \mathcal{H}_e the electrical alignment to the external field, namely,

$$\mathcal{H} = -\sum_{\langle i,j\rangle} J_{ij} \mathbf{p}_i \cdot \mathbf{p}_j + \sum_{\langle i,j\rangle} \mathbf{D}_{ij} \cdot (\mathbf{p}_i \times \mathbf{p}_j) - \sum_i \mathbf{E} \cdot \mathbf{p}_i, \quad (1)$$

where \mathbf{p}_i is the *n*-component spontaneous polarization distribution of the domain in the "ith" site with discrete values $\mathbf{p}_i = (\pm p_x, \pm p_y)$, $J_{ij} = JA_{ij}$ are the elements of the $N \times N$ adjacency matrix \hat{A} , with J the global coupling strength, and $\mathbf{D}_{ij} \propto \mathbf{p} \times \mathbf{e}_{ij}$, where \mathbf{e}_{ij} is the unit vector pointing from ith site to jth site and \mathbf{p} the polarization vector [31]. The last term corresponds to an applied external field and is described, as usual, as $\mathcal{H}_e = -\sum_i \mathbf{E} \cdot \mathbf{p}_i$.

A first-order parameter is taken to be the modulus $|\mathbf{p}|_i$ of the polarization in each direction $P = \frac{1}{N} \sum_i |\mathbf{p}|_i$, where i represents the sum over nodes, and $|p| = \sqrt{p_x^2 + p_y^2}$. A second-order parameter is taken to be $v = \frac{1}{2N} \sum_{\langle i,j \rangle} \frac{|\mathbf{p}_i \times \mathbf{p}_j|}{|\mathbf{p}_i||\mathbf{p}_j|}$, this

quantifying emergent rotational order in the system (i.e., vortexlike structures). This is an angular order parameter that captures the angular ordering of the system. Note that, unlike low-dimensional systems undergoing a continuous symme-

try breaking, where the emergence of topological defects in the form of vortices is expected as a direct consequence of the Mermin-Wagner theorem [34,35], for the present discrete symmetry case, vortexlike patterns are a direct consequence of the DMI.

Dipole-dipole-like interaction is analyzed using the lattice illustrated in Fig. 1(b), a 2D lattice based on a specific underlying mesoscopic arrangement, known as supercrystals (SCs), observed in a large variety of ferroelectrics [11,12,36] and other functional materials [37]. Here, the elementary triangular building block encompasses both type (i) and type (ii) walls with their protected flux-closure patterns, while the resulting structural geometry allows a nonvanishing DMI interaction, excluded in structures that have bond-inversion symmetry (such as square lattices [38]; see also the Supplemental Material [39]).

II. RESULTS

A. SC-tiling intrinsic scales

The intrinsic scales of the SC-tiling lattice are analyzed using the recent framework proposed in Refs. [40–42] (see Appendix A and the Supplemental Material [39]). The spectral analysis of the SC lattice is based on the time-evolution operator $e^{-\tau \hat{L}}$ of the diffusion or heat equation, where $\hat{L} = \hat{D} - \hat{A}$ is the Laplacian operator, \hat{A} the adjacency matrix, and \hat{D} the diagonal degree matrix [41]. Hence, one can define the Laplacian density matrix $\hat{\rho}(\tau) = \frac{e^{-\tau \hat{L}}}{Tr(e^{-\tau \hat{L}})}$ (see also Appendix A) to analyze the so-called lattice "heat capacity" [41] as $C(\tau) \equiv -\frac{dS}{d\log \tau}$, which describes the rate of information acquired about the network or lattice structure during diffusion dynamics at scale τ . In analogy with statistical physics, peaks of C are associated with structural phase transitions. Thus, we can analyze C at varying τ to investigate the lattice multiscale organization.

Figure 1(c) shows the so-called specific heat (C, seeAppendix A) of the SC structure. Along with the plateau that reflects the 2D nature of the lattice, as $C = \frac{d}{2}$ for scale-invariant architectures [42], C presents two possible small-scale modes or ultraviolet cutoffs (in the jargon of the renormalization group), Λ_1 and Λ_2 , independent of the system size, plus a third peak at larger values of τ reflecting the whole lattice scale. Compared to a regular 2D lattice that only presents two peaks, here, the extra peak plays, as discussed below, a key role in determining, altering, and disrupting the phases and phase transitions of the system. The presence of multiple characteristic topological scales (Λ_1 and Λ_2), each associated with a different type of interaction (Heisenberg- versus DM-like), leads to frustration: if the system cannot simultaneously minimize both energy terms globally. As a consequence, domains settle into configurations that are locally stable but globally incompatible—a hallmark of frustrated systems. This manifests in metastability, slow dynamics, and history-dependent responses (see below).

B. Phase diagram

Figure 2(a) shows the temperature phase diagram of the system as a function of the ratio between the dipole-dipole

alignment interaction J and the DMI, D. Results are achieved through extensive Monte Carlo simulations of the TBM, running Eq. (1) on top of the SC-tiling. In order to reach zero local charge density, the constraint $\nabla \cdot \mathbf{p}_{\Lambda_1} = 0$ is imposed as the energy is minimized [see Fig. 1(b)], centering it on each "plaquette" (the elementary protected cell Λ_1) to avoid nonphysical situations (see the Supplemental Material [39] for case examples of microscopic configurations, resembling the ice rule in spin-ice systems [43]). Inspection of the phase diagram reveals two stable collective dynamical regimes: vortices and ferroelectric phases. In particular, the microscopic scale Λ_1 now supports the existence of an ordered domain mosaic of 2D protected vortex cores. Different types of bifurcation lines separate the phases of the system. In particular, for low temperatures, increasing the ratio J/D, a first-order phase transition separates the vortex phase from the ferroelectric one. Conversely, a second-order phase transition separates the vortex phase from the paraelectric one. Interestingly, an intermediate phase emerges between the ferroelectric and paraelectric phases: A metastable, or frustrated, phase where transient vortices prevent the system from reaching a global order as in the ferroelectric or vortex phases, sequentially changing the full system orientation (see Appendix B).

Figures 2(b) and 2(c) show order parameters as a function of the temperature for the polarization P and vortex v for two different values of the ratio J/D. Note that P and v correctly detect the stable ordered phases. Insets show the anomalous temporal fluctuations σ_P^2 and σ_v^2 , which exhibit a pronounced peak located at the (N-dependent) transition point between the different phases. In particular, the broad divergence of σ_P^2 is a hallmark of frustrated phases in statistical mechanics, supporting the picture of broad criticallike regions [44,45], and gives us a marker for the emergence of an intermediate phase between the ferroelectric and the paraelectric ones (see also Appendix B).

Findings are compared to experiments in SCs observed in KTN:Li crystals (see also Appendixes C and D). This material, which led to the first observation of wave replicasymmetry breaking [46], has been developed by several groups [47–50] as a lead-free optically transparent alternative to other commonly used perovskites [51]. Moreover, compared to commercially available crystals, such as BTO (Barium Titanate) [37] and STN (Strontium Barium Niobate) [52], it has tunable properties with a room-temperature ferroelectric transition [8,53,54]. Fourier computational analysis of the vortex phase (see also the Supplemental Material [39]) is found to match observed optical far-field results, as shown in Fig. 2(d), in agreement with the previous SC models based on an interlocked regular structure of spontaneous polarization [6,54,55]. The TBM model then provides a feasible explanation to why the SC phase appears only in some specific materials, as the internal structure must be fine-tuned to present a specific J/D ratio.

C. The effect of a bias electric field

Response to a bias electric field is analyzed theoretically by adding the term $\mathcal{H}_e = -\sum_i \mathbf{E} \cdot \mathbf{p}_i$ in Eq. (1). As reported in Fig. 2(e), the temperature versus electric field phase diagram presents a rich phenomenology. At low temperatures,

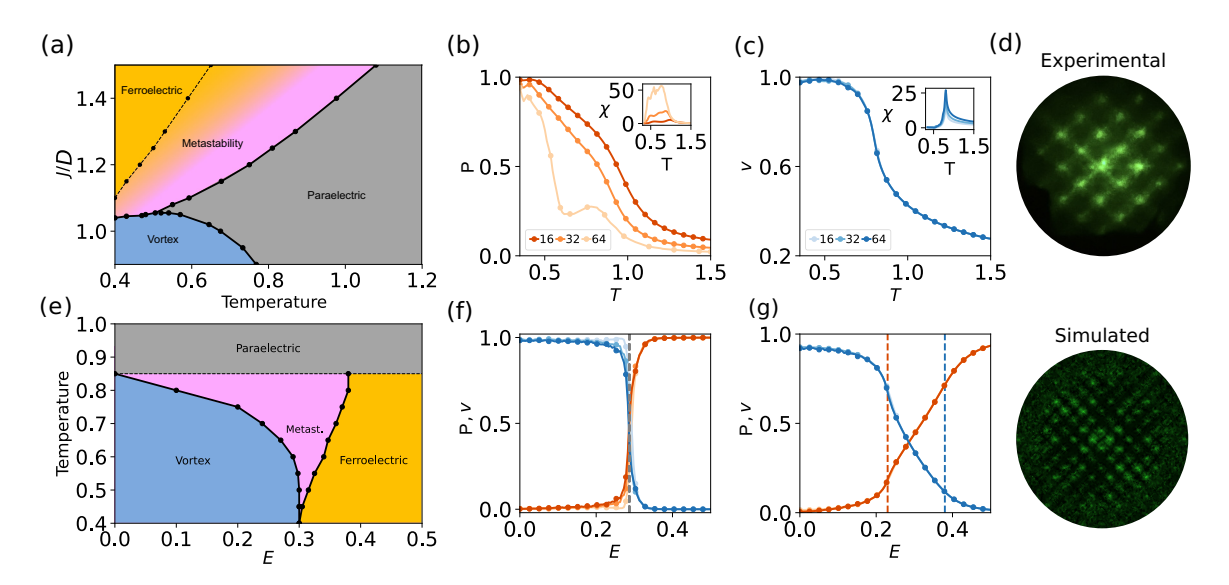


FIG. 2. Topological symmetry breaking. (a) Temperature phase diagram of Eq. (1) computed using direct simulations on an SC lattice with N = 1024 nodes (J = 1). Polarized states are computationally detected with the polarization order parameter P, while vortex phases are detected through the vortex order parameter v. The metastable phase corresponds to the broad region of divergent polarization susceptibility $\chi_P = N\sigma_P^2$. Polarization (P) and vortex (v) order parameters vs temperature for different lattice sizes (see legend, $N = 4L^2$) for (b) J/D = 1.4 and (c) J/D = 0.8. Inset: Rescaled temporal variance $\chi_P = N\sigma_P^2$ vs temperature T for different system sizes. The metastable phase also presents characteristic temporal oscillations in the global system polarization (see Appendix B). (d) Top: Far-field imaging of an SC structure at $T = T_C - 2$ K. Bottom: Computational 2D Fourier transform of an ordered vortex phase (J/D = 0.8, T = 0.4, N = 1024). (e) Temperature phase diagram of the model vs electric field E for J/D = 0.8 and N = 1024 nodes. The breakup of the vortex phase translates into the emergence of a metastable phase where the ferroelectric and vortex domains naturally coexist. Polarization (P) and vortex (v) order parameters as a function of the electric field for different lattice sizes [as in panels (b) and (c)] for (f) T = 0.4 and (g) T = 0.7. The peak in the system susceptibility is indicated here as a vertical dashed line. Note how the critical field at low temperatures splits into two different phase transitions when T increases, with naturally coexisting vortices and ferroelectric domains. All curves have been averaged over 10^2-10^3 independent realizations.

the vortex phase is separated from the ferroelectric phase by a first-order phase transition, while the critical temperature T_p gives rise to the paraelectric phase (dashed lines). Far below this temperature, a different metastable or frustrated phase emerges in contrast to the previous case. As before, the order parameters (P and v) characterize the phase transitions as a function of the external field, as shown in Figs. 2(f) and 2(g).

Cluster patterning is directly observed using laser light cross-polarizer transmission microscopy [56] (see Appendix C for a detailed description of the experimental setup). Specifically, light propagating in the SC structure becomes depolarized and hence is able to pass through the crossed polarizers [57]. Regions where no transmission is observed identify where the SC either is not formed or has a defect, such as in proximity of a domain wall. Basic phenomenology and analysis are reported in Fig. 3, showing the transition from light transmission, partial, to no light transmission as the SC structure is caused to break down. Increasing the bias field for a sample cooled to $T_C - 4.5 \,\mathrm{K}$, at $E_c = 2.91 \,\mathrm{kV/cm}$ the crossed-polarizer image suddenly becomes opaque, indicating SC breakup and an ensuing overall depolarized transmitted beam [see Fig. 3(a)]. Polarization transmission images have been selected to show the percolative nature of the observed phenomena at three different temperatures below $T_C = 294 \,\mathrm{K}$, and for different electric field values E, as shown in Fig. 3(b). For temperatures up to $T_C - 3.5$ K, the SC no longer manifests sudden polarization changes. Transmission starts to decrease along particular directions, oriented at 45° relative to the crystal principal axes. Bias-induced distortions are found to predominantly affect the SC structure along these inclined paths, at the critical field value $E_c = 2.81 \, \mathrm{kV/cm}$. Despite this, light transmission remains evident in the overall image. A different behavior is found at $T_C = 2.5 \, \mathrm{K}$. Specifically, while analogous SC distortions appear along inclined paths, but at a lower field, $E_c = 2.5 \, \mathrm{kV/cm}$, as the bias is increased, the darker regions are observed to expand along these specific directions until they cover the entire transmitted image at $E_c = 2.86 \, \mathrm{kV/cm}$ (see Appendix E), as seen at $T_C = 4.5 \, \mathrm{K}$.

The phase transition can be characterized through the usual percolation order parameter $P_{\infty} = n_{\infty}/N$, where n_{∞} is the number of pixels belonging to the largest cluster and N is the total number of pixels in the processed image [56]. The images are binarized by applying an arbitrary threshold intensity θ . Each pixel in the image is classified into one of two states, i.e., one or zero, based on whether its intensity is below or above the threshold, respectively. Hence, the largest cluster of light corresponds to the intensity in Fig. 3, with the electric field E as the control parameter, showing a percolation phase transition at some critical value E_c . We note that the proper identification of the translational invariant "building blocks" justifies the dynamical analysis of the system on a coarsegrained scale that can potentially alter the system universality class, as found when the system is biased with an electric field.

Figures 3(c)-3(e) show the percolation phase transition for all three selected temperatures below T_C and different values of θ . Experimental results are fully compatible with

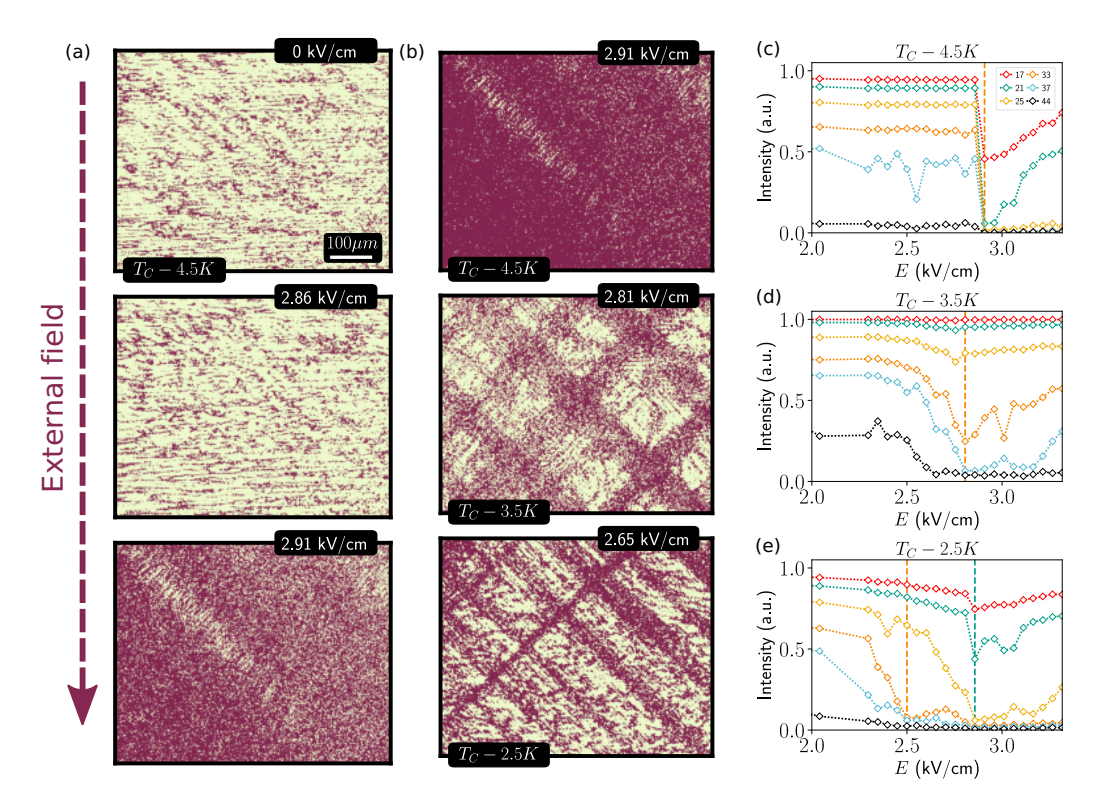


FIG. 3. Direct imaging of SC ferroelectric clusters. Binarized crossed-polarizer transmission microscopy images for (a) $T_C-4.5$ K and increasing electric field (0, 2.86, and 2.91 kV/cm, respectively, using $\theta=25$). Light transmission shows an abrupt transition at $E_C\approx2.9$ kV/cm. (b) Various conditions of temperature and bias electric field to enhance the critical point for the first two temperatures and the metastable region for $T_C-2.5$ K (see images, with $\theta=37,37$, and 35, respectively). Light intensity vs applied electric field (E) for three different temperatures and different threshold values (θ , see legend): (c) $T_C-4.5$ K. An abrupt phase transition is present at a field $E_C\approx2.9$ kV/cm for a wide range of θ values. (d) $T_C-3.5$ K. The abrupt transition changes its nature to a continuous one with $E_C\approx2.75$ kV/cm. (e) $T_C-2.5$ K. The system exhibits two different phase transitions at different critical fields, $E_C\approx2.5$ kV/cm and $E_C\approx2.86$ kV/cm (see also Appendix E).

numerical results reported in Figs. 2(e)–2(g). For temperatures deep into the ferroelectric phase, $T_C - 4.5$ K, and $T_C - 3.5$ K, the system shows a first-order phase transition that splits into two phase transitions for $T_C - 2.5$ K (at $E_c = 2.5$ and $E_c = 2.86$, respectively). Besides, the nature of the phase transitions changes between Figs. 3(c) and 3(d), the latter being more likely in the vicinity of some triple point. Note also how the original first-order phase transition (orange dashed lines in Fig. 2) shifts toward lower fields as expected from our theoretical framework.

To establish whether the TBM actually supports a percolative phase transition, we analyzed each unit belonging to the microscopic scale, Λ_1 , on a coarser scale: each blockdipole now represents a node that either allows light to pass $(\ell = 1)$ or does not $(\ell = 0)$. This embodies the idea that for the KTN:Li, only the SC vortex phase allows complete light transmission. The giant cluster P_{∞} characterizes the phase transition, together with the susceptibility $\chi(h) = \frac{\sum_{S} S^2 P(S,h)}{\sum_{S} SP(S,h)}$ Here, the sum runs over all possible cluster sizes S for a given field h in the system, P(S, h) being the cluster size probability distribution, and discarding P_{∞} , if it exists. Figure 4(a) shows the percolation phase transition at low temperatures, which confirms that an abrupt phase transition occurs at a specific critical field E_c . Figure 4(b) illustrates the behavior in the metastable phase, shedding light on two key properties: (1) the phase transition in the metastable region is found to be smoother and (2) susceptibility diverges throughout the entire region. Figure 4(c) shows different states when the external field increases. At low temperatures, labyrinthinelike structures form where ferroelectric domains start to aggregate, giving rise to a giant cluster that spans the entire system at a critical field E_C . This leads to the frustrated phase, where both the vortex and ferroelectric mesoscopic domains coexist in an interlocked way, forming fractal patterns [see Fig. 4(c)].

Macroscopic response is analyzed in Fig. 5, where the behavior of P_{∞} versus applied field is reported. The orange loop refers to the temperature where frustration is absent, leading to a strongly hysteretic response function typical of a first-order transition. In contrast, a slim loop (violet loop) emerges in the metastable phase, a signature of negligible hysteresis and marked nonlinearity. Characteristic discrete jumps in polarization (see the enlarged inset in Fig. 5) are caused by the depinning of finite domains, the so-called Barkhausen jumps in hysteretic loops [7,58].

III. DISCUSSION

A knot in a string is a remarkably stable physical form of information storage since it is topologically protected; that is, it can only be erased by untangling it [59–62]. Knotlike structures emerge naturally in the form of topological defects in a wide variety of materials [63], such as liquid crystals [64], fluids [65], ferromagnets [66,67], and ferroelectrics [13,14].

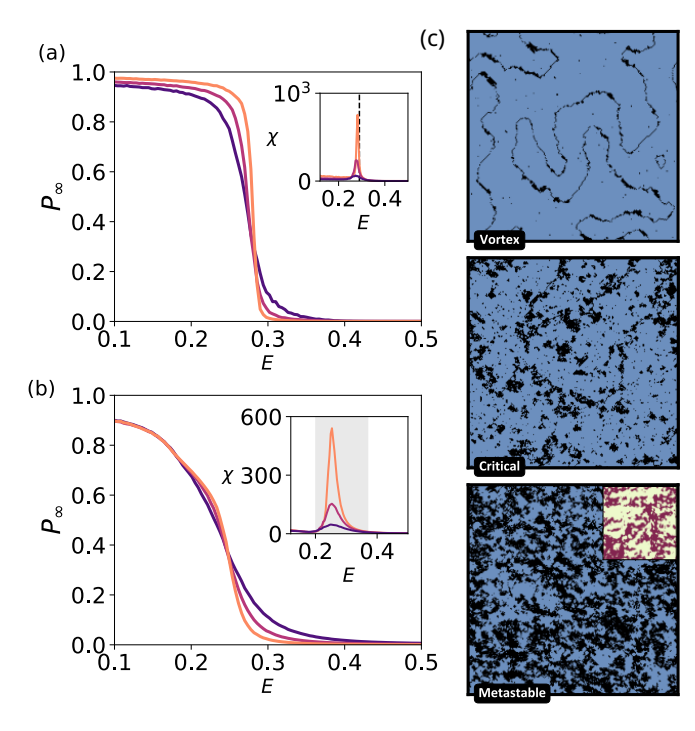


FIG. 4. Percolation phase transition. P_{∞} as a function of the applied field E for different system sizes (in the square lattice of side L resulting from the coarse-graining process; see legend) for (a) T=0.4. Inset: χ vs E. Note the divergence at a specific point as the system size increases. (b) T=0.75. Inset: χ vs E. Note the divergence of the entire metastable region as the system size increases. (c) Configurations of simulated light transmission images. From up to down, images show a vortex state (T=0.4, E=0.2), the bifurcation line to the metastable phase (T=0.5, E=0.29), and the metastable phase (T=0.5, E=0.3). For the sake of comparison, the inset shows an enlarged region of experimental light transmission at $T_C = 0.5$ K and $T_C = 0.5$ K and $T_C = 0.5$ K and $T_C = 0.5$ K.

This protection is responsible for the stability of intricate low-dimensional topological polar structures (e.g., quadrant domains [68], polar flux closures [16,69,70], and vortices [71]) that, in recent years, have attracted significant attention [11,12,72]. Analogous topologically protected patterns naturally occur in a wide variety of systems [63], such as liquid crystals [64], fluids [65], and ferromagnets [66,67]. Among these, topologically protected ferromagnetic skyrmions [73] have found applications in electromechanical and spintronic devices for information storage [74] and logic [75].

At present, the potential of topological defects as noise-resistant memory and processing elements is largely unexplored, especially because their behavior appears intimately connected with an intriguing but little understood frustration in the hosting material [15,76,77]. In some respects, frustration likens functional materials, such as ferroelectric crystals, to the large class of information-driven phenomena, such as memory effects [78], protein-folding mechanisms [79], brain dynamics [45,80], and slow relaxation dynamics [81]. The driving mechanism for frustration is commonly thought to be an underlying disorder that can, for example, influence a conventional phase transition by introducing competing interaction terms between multiple components and lead to frustration [4]. In ferroelectrics, complex behavior is typically

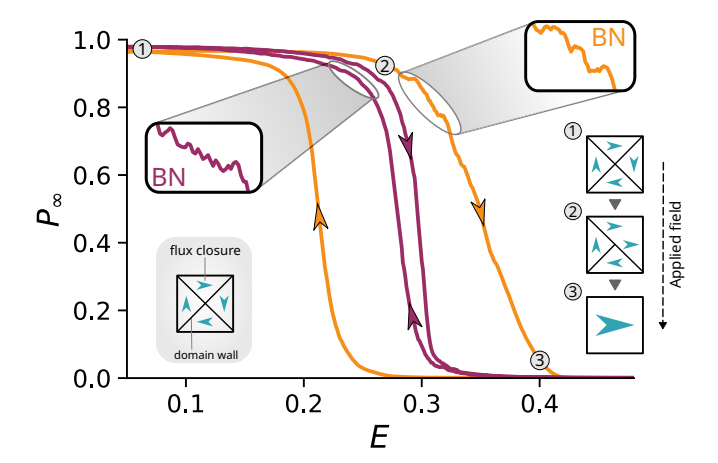


FIG. 5. Slim-loop hysteresis. P_{∞} as a function of the applied field E for different temperatures T=0.4 (orange line) and T=0.6 (violet line) for a lattice with L=64 coarse-grained units. The wide hysteretic behavior at low temperatures, characteristic of the first-order phase transition, becomes a slim-loop hysteresis cycle in the intermediate phase. The break of domain walls on pinned sites originates the observed jumps in the hysteretic cycle, that are shown in the zoomed insets. This gives rise to the well-known Barkhausen noise.

attributed to alterations in what would normally be considered a conventional paraelectric-ferroelectric structural phase transition caused by built-in compositional disorder. Disordered ferroelectrics can be modeled as a system dominated by mesoscopic polar nanoregions (PNRs), regions originally thought to have randomly distributed dipole moments driven by exchange interaction [7,82,83], that have more recently been shown to manifest a hierarchical structure with no sudden boundaries [20]. Complex behavior could then be explained as an analog of Griffiths phases theoretically predicted long ago (but not yet experimentally found) for dilute ferromagnetic systems [84]. This approach has been demonstrated to be insufficient at temperatures lower than the Curie temperature (T_C) because it fails to consider PNR interaction [2]. The existence of a glassy state has also been proposed as an alternative explanation [1,85]. Glassy approaches, in turn, encounter difficulties in describing some of the basic observed features, such as the occurrence of Barkhausen jumps during the poling process, jumps that are incompatible with the continuous and monotonous glassy reorientation of dipoles on submicrometer length scales [7]. A complete understanding of emergent relaxor behavior in disordered ferroelectrics remains an open problem [86].

Our study suggests an altogether different picture. Here, built-in disorder is relegated to generating the SC-tiling and plays no direct role in the TBM. Yet, the approach is able to reproduce the signature and hereto little understood complex and nonergodic behavior of disordered ferroelectrics like KTN.

Hence, the percolative transition typical of relaxor-like perovskites [56,77,87] is predicted by the TBM at low temperatures (below T_C) as an abrupt phase transition that splits into two critical electric fields with an intermediate behavior that resembles that of the frustrated phase presented here (as discussed in Figs. 3 and 4). We note that while the

cubic-to-tetragonal transition model used here is a useful paradigm for many perovskite ferroelectrics, other systems like PMN and BTO may exhibit more complex or distinct symmetry-breaking behavior. Nonetheless, our model captures the general interplay between discrete-inversionsymmetry breaking and charge-screening-driven topology, which remains relevant across a wide class of materials. Moreover, as discussed in Fig. 5, the TBM is able to describe the anomalous hysteretic "slim-loop" behavior observed in relaxor behavior, along with the characteristic Barkhausen jumps [7]. Our results indicate that complexity-driven phenomenology originates from the competition between the two intrinsically different scales (Λ_1 and Λ_2) that arise not out of disorder but geometrically, from the interaction terms of Eq. (1), as discussed in Fig. 1, leading to local energetic incompatibilities that persist even in the thermodynamic limit.

Hence, the interplay between the Heisenberg- and DMI-like terms naturally introduces frustration into the system. These two interactions, effective at different spatial scales, cannot be simultaneously minimized. We want to emphasize that other types of interactions, grounded in different topological scales as supported by the SC lattice, may also lead to similar effects. As a result, the system is unable to achieve a globally ordered state, leading to the emergence of metastable regimes characterized by local competition between polarized and vortex domains. This frustration is intrinsic to the TBM and forms the basis for the rich phase behavior discussed here.

The idea that exotic states with degenerate energy surfaces and broad critical phenomena can arise from the breaking of a regular structure of topologically protected states, i.e., the topological symmetry-breaking transition discussed in Figs. 3 and 4, presents a route for future experiments and applications. For example, in distinction to spin-glass systems, here the nonergodic metastable phase is characterized by an intriguing state with localized regions of topologically protected patterns, each pattern then forming a potentially noise-resistant memory cell. Notably, a slight reduction in accuracy enhances memory capacity while preserving a large set of protected structures. This trade-off is particularly advantageous for machine learning purposes, where a larger parameter space allows for encoding more information without requiring perfect accuracy.

Finally, we note that the TBM addresses the issue of describing ferroelectric behavior dominated by compositional disorder that leads to interacting mesoscopic domains relevant to optical propagation. In this regime, structural analysis and molecular dynamics simulations can prove challenging. Indeed, the TBM is not intended to fully replace detailed microscopic simulations, such as phase-field or ab initio approaches. Rather, it provides a minimal and analytically tractable framework to explore how competing mesoscopic interactions and geometric constraints can produce complex, nonergodic behavior. The simplicity of the model allows insight into qualitative mechanisms that may remain hidden in fully numerical treatments. Qualitatively, the TBM isolates key mechanisms that can lead to complex domain phases in functional materials. In line with efforts to formulate minimal yet effective theories that capture essential physics with maximal simplicity [88], the TBM reveals that it is the competition between effective dipole-dipole-like interactions and the intrinsic two-scale lattice geometry that drives the formation of such intricate domain structures. While KTN:Li is used here as a case study, the TBM is generic and applicable to other polar materials with flux-closure behavior and competing dipolar interactions that manifest superlattices. Future studies could explore applications to, e.g., SBN or multiferroic materials.

IV. CONCLUSIONS

Concluding, we have introduced and experimentally validated an explanatory framework for complex behavior observed in disordered ferroelectric crystals that support superlattices, such as KTN. Emergent phenomena are found to be a consequence of the competition between two basic topological defects that emerge from the spontaneous breaking of discrete-inversion symmetry and volume-charge screening: domain walls parallel to the principal crystal axes, across which the polarization flips by 180°, and slanted at 45°, across which the polarization abruptly rotates by 90° [16,17,89]. Frustration is then triggered by the interplay between the two corresponding spatial scales, each with its specific dipole-dipole interaction, a Heisenberg- and a DM-like interaction. The mechanism leads to vortex and metastable phases, depending on the ratio of the two underlying interaction components. The application of the real-space renormalization group methods to detect domain patterns reveals the existence of a frustrated percolation phase transition that naturally includes depinning effects, i.e., domain wall reorientation that results in the well-known Barkhausen jumps and slim-loop hysteretic phenomena, when topologically protected states are broken. Our expansion of classical frustration mechanisms, beyond spin-glass and Griffiths effects, opens a route to explore the intriguing interplay between structure and dynamics and how this can give rise to previously unknown phases, potentially rising to a level the design and development of innovative miniaturized noise-resistant highperformance information and energy storage devices [90].

ACKNOWLEDGMENTS

L.F. and E.D.R. acknowledge support from PNRR MUR Projects No. PE0000023-NQSTI, No. PRIN 2022 MUR Project No. 20223T577Z, and Sapienza-Ricerca di Ateneo Projects. P.V. acknowledges the Spanish Ministry of Research and Innovation and Agencia Estatal de Investigación (AEI), Grant No. MICIN/AEI/10.13039/501100011033, for financial support through Project No. PID2023-149174NB-I00, funded also by European Regional Development Funds, as well as Ref. PID2020-113681GB-I00. A.J.A. acknowledges support from the Ministry of Science, Technology and Space (IL Grant No. 4698). We thank A. Gabrielli for extremely valuable discussions and suggestions on earlier manuscript versions.

DATA AVAILABILITY

The data that support the findings of this article are not publicly available. The data are available from the authors upon reasonable request.

APPENDIX A: STATISTICAL PHYSICS OF INFORMATION NETWORK DIFFUSION

The Laplacian $\hat{L} = \hat{D} - \hat{A}$ governs the diffusion dynamics on any regular or heterogeneous structure through the equation

$$\dot{\mathbf{s}}(\tau) = -\hat{L}\mathbf{s}(\tau),$$

where $\mathbf{s}(\tau)$ represents, for instance, the information distribution on the network nodes, \hat{D} is the degree matrix, and \hat{A} is the structure's adjacency matrix. The general solution for this equation is $\mathbf{s}(\tau) = e^{-\tau \hat{L}} \mathbf{s}(0)$. This leads to the concept of Laplacian density matrix, $\hat{\rho}(\tau) = \frac{e^{-\tau \hat{L}}}{Tr(e^{-\tau \hat{L}})}$, which makes it possible to analyze network structures in greater detail [40,41], opening the door to a thorough analysis through the introduction of the Laplacian entropy, $S(\tau) = -\frac{1}{\log N}\hat{\rho}(\tau)\log\hat{\rho}(\tau)$, and the entropic susceptibility (or specific heat). The "canonical" description of heterogeneous networks in analogy with statistical mechanics [40,41] is rigorously supported because \hat{L} plays formally the role of a Hermitian (lower-bounded) Hamiltonian, $Z(\tau)$ is the partition function, and τ is a control parameter akin to the inverse temperature.

In particular, it is the temporal derivative of the entropy, which has been denominated the heat capacity of a network [41],

$$C(\tau) = -\frac{dS}{d(\log \tau)},$$

as the natural counterpart of the specific heat in classical statistical mechanics. In particular, C is a detector of structural transition points corresponding to the intrinsic characteristic diffusion scales of the network [40,41]. Indeed, a pronounced peak of C defines $\tau = \tau^*$ and reveals the starting point of a strong deceleration of the information diffusion, separating regions sharing a rather homogeneous distribution of information from the rest of the network. Finally, in the continuum approximation of the Laplacian spectrum, it has been recently proved that the exponent γ satisfies the following relation [40,42]:

$$C_1 = \frac{\Gamma(\gamma + 2)}{\Gamma(\gamma + 1)} = \gamma + 1 = \frac{d_s}{2},$$

where $\Gamma(z)$ is the Euler's gamma function, and the plateau corresponds to half of the spectral dimension d_s of the network or lattice [42].

APPENDIX B: EXPLORING THE METASTABLE PHASE

For completeness, we present numerical results for the temporal evolution of the polarization order parameter P. Our results reveal the existence of such a metastable regime placed between the vortex and the ferroelectric phase. This is characterized, as shown in Fig. 6, by broad quasiperiodic temporal oscillations of P.

Anomalously large sampling times would be required to extract good statistics for the actual mean values and variances. This collective behavior is a straightforward manifestation of the partial ordering of the system, being

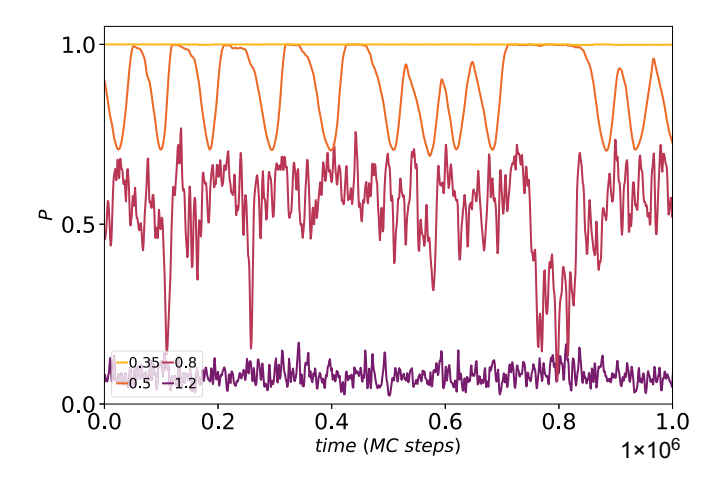


FIG. 6. Temporal variability. Polarization order parameter (P) as a function of time (in Monte Carlo steps). Different colors represent different values of T (see legend). The broad variability characterizing the metastable phase wildly depends upon the initial conditions for each realization. Parameters: J/D = 1.4 and L = 32.

reminiscent of other types of nonergodic behavior in structured systems [44,80] but with a completely different origin.

We also report different snapshots of the system configurations for multiple phases here to illustrate the emergent order in the two-scale SC lattice. These snapshots have been selected by varying the ratio J/D and the temperature T. Figure 7(a) illustrates the vortex phase, while Figs. 7(b) and 7(c) show two metastable configurations corresponding to two different temperatures on the phase diagram reported in the previous sections.

APPENDIX C: EXPERIMENTAL SETUP

Laser light from a doubled 30 mW Nd:YAG laser (wavelength $\lambda = 2\pi/k_0 = 532$ nm) is made to propagate along the z axis through the zero-cut KTN:Li crystal sandwiched in between two crossed polarizers. The sample is biased by a time-constant electric field E along the x axis. The crystal temperature T is set by a current-controlled Peltier junction in contact with one of the y facets. Light from the crystal output facet is imaged using a movable spherical lens L1 (of focal length 50 mm) onto a CMOS camera. The crosspolarizer technique implemented utilizes the birefringence of polar clusters to alter the polarization state of light, allowing optical observation of microscopic cluster dynamics at micrometer scales. The experimental setup is illustrated in Fig. 8.

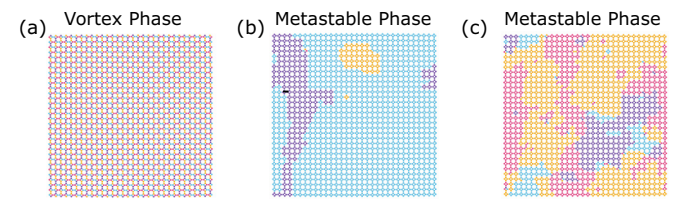


FIG. 7. Snapshots of several domain arrangements for different phases. (a) J/D=0.8, T=0.35, (b) J/D=1.4, T=0.5, and (c) J/D=1.4 T=0.8. Parameter: L=32.

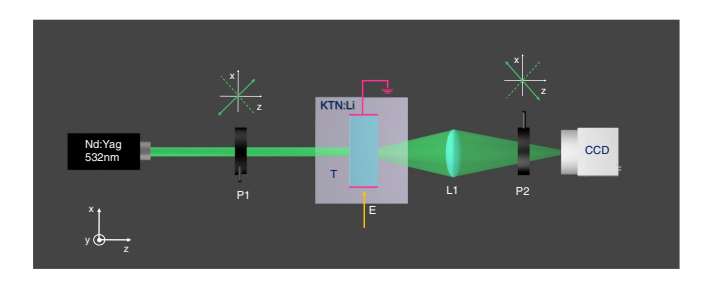


FIG. 8. Experimental setup. Scheme of the cross-polarizer transmission microscopy setup used to resolve mesoscopic polarization textures in KTN:Li.

APPENDIX D: MATERIAL

The sample is a zero-cut optical quality polished lithium-enriched solid solution of potassium-tantalate-(KTN:Li) with an average composition $K_{0.964}Li_{0.036}Ta_{0.60}Nb_{0.40}O_3$. Its dimensions are $2.33^{(x)} \times$ $1.96^{(y)} \times 2.03^{(z)} \, \text{mm}^3$. The unit cell manifests random substitutions, a compositional disorder that, as a consequence of the structural flexibility typical of perovskites, leads to locally modified polarizabilities and temperature-dependent nanoscale dipolar structures (nanodisordered ferroelectricity). The result is a modified ferroelectric behavior dominated by the so-called PNRs, characterized by dielectric dispersion and out-of-equilibrium behavior (relaxor ferroelectricity) [3]. In our present case, this disorder is itself not homogeneous, manifesting a spatially periodic micrometric oscillation along a specific crystal axis. This is because the sample is grown into a bulk through the top-seeded method, a technique that entails a slight time oscillation in the temperature of the solidifying melt that, in turn, translates into an approximately periodic 7.5 µm pattern along the growth (or pull) axis, which causes in ferroelectrics an equally patterned T_C . This pattern conditions the nanoscale dipolar structures that, at the room-temperature Curie point $T_C = 295 \,\mathrm{K}$, form an orderly multidomain protected regular state, the SC [6,8,56,57]. SCs are thought to originate in a regular lattice of interlocked polarization vortices, a generalization of the spontaneous polarization closed-flux vortex domain pattern dominated by a triangular tiling, compatible with available experimental results and phase-field simulations [6]. This arrangement effectively screens the polarization charge and elastic stress [8,91]. SC phase also manifests striking optical properties, such as giant broadband refraction (GR) [53,55] and constraint-free wavelength conversion [54].

APPENDIX E: PERCOLATION ANALYSIS OF SC STRUCTURES

Basic phenomenology is reported in Fig. 9, where polarization transmission images through the sample are shown for various temperatures below $T_C = 294 \,\mathrm{K}$ and different external electric fields E. In pure depoled ferroelectrics, random birefringence causes complete depolarization of propagating optical fields, resulting from multiple interferences of randomly scattered waves. In contrast, light propagating in an SC

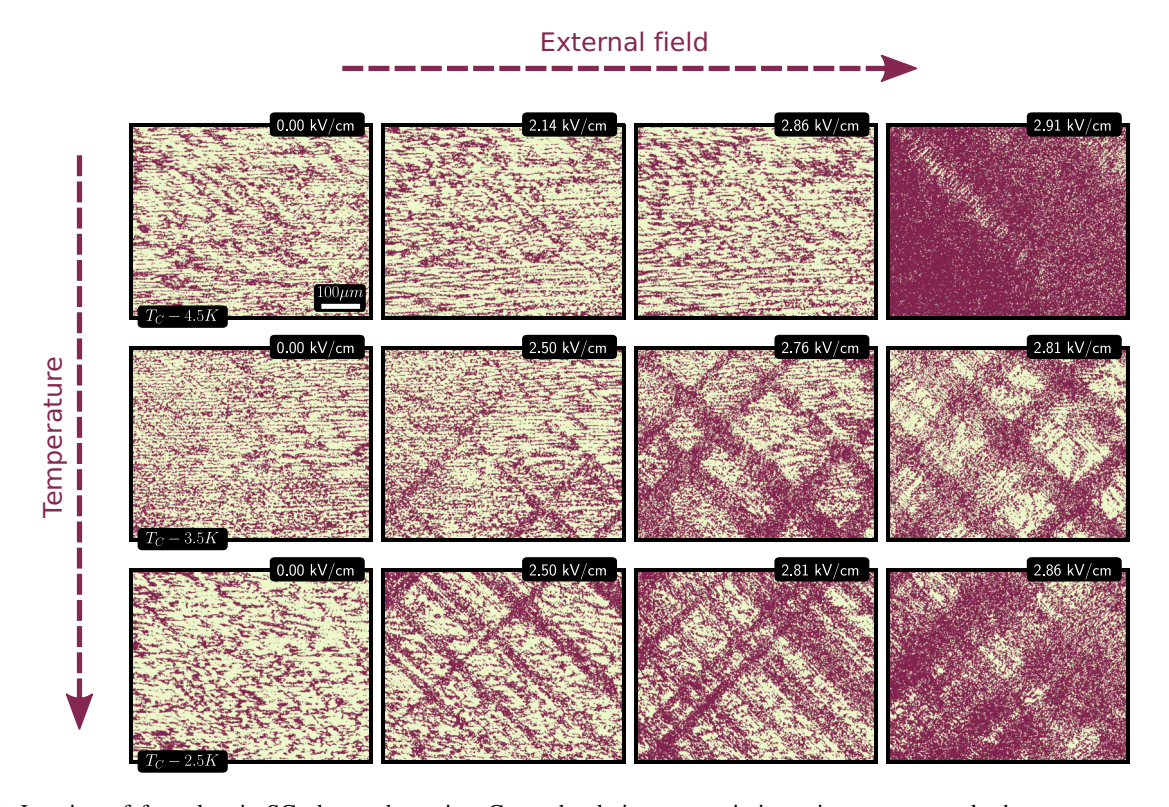


FIG. 9. Imaging of ferroelectric SC cluster dynamics. Crossed-polarizer transmission microscopy reveals the temperature- and field-dependent breakdown of the SC phase in KTN:Li. The images highlight the emergence of percolative transitions and anisotropic distortions aligned at 45° to the crystal axes, marking the onset of metastable vortex-ferroelectric coexistence predicted by the topological breakdown model.

suffers a GR, where waves travel along the principal axes of the crystal without diffracting, remaining fully polarized for a linear polarization along the SC principal axes [57]. The result is that the transmitted light at the output will be a checkerboardlike polarization pattern, with alternating orthogonally polarized states (see Fig. 9 for E=0). This naturally amounts to a natural 3D orthographic projection, opening the possibility of observing optically the microscopic details of SC cluster dynamics even though it is taking place on the micrometer scale in a full 3D volume [56]. Supporting the main text, in Fig. 9, a more detailed phenomenology is reported, where polarization transmission images through the sample are shown for various temperatures below $T_C=294\,\mathrm{K}$ and different external electric fields E. The sudden transition at

 $T_C-4.5$ K evolves into a much richer phenomenology, fully compatible with our hypothesis of an emergent metastable phase. In fact, for a temperature up to $T_C-3.5$ K, the SC does not show any more sudden polarization changes. Crossed-polarizer transmission starts to decrease along particular directions, oriented at 45° relative to the crystal principal axes ($E_c=2.81$ kV/cm). Despite this, light transmission remains evident in the overall image. Increasing temperature further ($T_C-2.5$ K), SC distortions appear at a lower field, $E_c=2.5$ kV/cm along the inclined paths, analogously to the previous case. As the bias field increases, the dark regions expand along these specific directions until they cover the entire transmitted image at $E_c=2.96$ kV/cm, analogously to the case at $T_C-4.5$ K.

- D. Viehland, S. Jang, L. E. Cross, and M. Wuttig, Freezing of the polarization fluctuations in lead magnesium niobate relaxors, J. Appl. Phys. 68, 2916 (1990).
- [2] A. A. Bokov, Ferroelectric domains and polar clusters in disordered structures, Ferroelectrics 190, 197 (1997).
- [3] A. Bokov and Z.-G. Ye, Recent progress in relaxor ferroelectrics with perovskite structure, J. Mater. Sci. 41, 31 (2006).
- [4] N. Choudhury, L. Walizer, S. Lisenkov, and L. Bellaiche, Geometric frustration in compositionally modulated ferroelectrics, Nature (London) 470, 513 (2011).
- [5] A. A. Bokov and Z.-G. Ye, Dielectric relaxation in relaxor ferroelectrics, J. Adv. Dielectr. **02**, 1241010 (2012).
- [6] F. Xin, L. Falsi, Y. Gelkop, D. Pierangeli, G. Zhang, F. Bo, F. Fusella, A. J. Agranat, and E. DelRe, Evidence of 3D topological-domain dynamics in KTN:Li polarization-supercrystal formation, Phys. Rev. Lett. 132, 066603 (2024).
- [7] V. Westphal, W. Kleemann, and M. D. Glinchuk, Diffuse phase transitions and random-field-induced domain states of the "relaxor" ferroelectric PbMg_{1/3}Nb_{2/3}O₃, Phys. Rev. Lett. 68, 847 (1992).
- [8] D. Pierangeli, M. Ferraro, F. Di Mei, G. Di Domenico, C. De Oliveira, A. Agranat, and E. DelRe, Super-crystals in composite ferroelectrics, Nat. Commun. 7, 10674 (2016).
- [9] T. Nishinaga, Handbook of Crystal Growth: Fundamentals (Elsevier, Boston, 2014).
- [10] A. Agranat, C. de Oliveira, and G. Orr, Dielectric electrooptic gratings in potassium lithium tantalate niobate, J. Non-Cryst. Solids 353, 4405 (2007).
- [11] V. Stoica, N. Laanait, C. Dai, Z. Hong, Y. Yuan, Z. Zhang, S. Lei, M. McCarter, A. Yadav, A. Damodaran *et al.*, Optical creation of a supercrystal with three-dimensional nanoscale periodicity, Nat. Mater. 18, 377 (2019).
- [12] M. Hadjimichael, Y. Li, E. Zatterin, G. A. Chahine, M. Conroy, K. Moore, E. N. O. Connell, P. Ondrejkovic, P. Marton, J. Hlinka *et al.*, Metal-ferroelectric supercrystals with periodically curved metallic layers, Nat. Mater. 20, 495 (2021).
- [13] I. Luk'Yanchuk, Y. Tikhonov, A. Razumnaya, and V. Vinokur, Hopfions emerge in ferroelectrics, Nat. Commun. 11, 2433 (2020).
- [14] V. Govinden, S. Prokhorenko, Q. Zhang, S. Rijal, Y. Nahas, L. Bellaiche, and N. Valanoor, Spherical ferroelectric solitons, Nat. Mater. 22, 553 (2023).

- [15] J. Junquera, Y. Nahas, S. Prokhorenko, L. Bellaiche, J. Íñiguez, D. G. Schlom, L.-Q. Chen, S. Salahuddin, D. A. Muller, L. W. Martin *et al.*, Topological phases in polar oxide nanostructures, Rev. Mod. Phys. **95**, 025001 (2023).
- [16] C. Kittel, Physical theory of ferromagnetic domains, Rev. Mod. Phys. 21, 541 (1949).
- [17] L. Landau and E. Lifshitz, On the theory of the dispersion of magnetic permeability in ferromagnetic bodies, Phys. Z. Sowjetunion **8**, 101 (1935).
- [18] K. M. Rabe, M. Dawber, C. Lichtensteiger, C. H. Ahn, and J.-M. Triscone, Modern physics of ferroelectrics: Essential background, in *Physics of Ferroelectrics: A Modern Perspective*, edited by M. Rabe, C. H. Ahn, and J.-M. Triscone (Springer, Berlin, 2007), pp. 1–30.
- [19] A. Gumennik, Y. Kurzweil-Segev, and A. J. Agranat, Electrooptical effects in glass forming liquids of dipolar nano-clusters embedded in a paraelectric environment, Opt. Mater. Express 1, 332 (2011).
- [20] M. Eremenko, V. Krayzman, A. Bosak, H. Playford, K. Chapman, J. Woicik, B. Ravel, and I. Levin, Local atomic order and hierarchical polar nanoregions in a classical relaxor ferroelectric, Nat. Commun. 10, 2728 (2019).
- [21] P. Gehring, H. Hiraka, C. Stock, S.-H. Lee, W. Chen, Z.-G. Ye, S. Vakhrushev, and Z. Chowdhuri, Reassessment of the burns temperature and its relationship to the diffuse scattering, lattice dynamics, and thermal expansion in relaxor Pb(Mg_{1/3}Nb_{2/3})O₃, Phys. Rev. B 79, 224109 (2009).
- [22] I. Muench, A. Renuka Balakrishna, and J. Huber, Periodic boundary conditions for the simulation of 3D domain patterns in tetragonal ferroelectric material, Arch. Appl. Mech. 89, 955 (2019).
- [23] Y. Yoshimura, K.-J. Kim, T. Taniguchi, T. Tono, K. Ueda, R. Hiramatsu, T. Moriyama, K. Yamada, Y. Nakatani, and T. Ono, Soliton-like magnetic domain wall motion induced by the interfacial Dzyaloshinskii-Moriya interaction, Nat. Phys. 12, 157 (2016).
- [24] Y. Ishikuro, M. Kawaguchi, N. Kato, Y.-C. Lau, and M. Hayashi, Dzyaloshinskii-Moriya interaction and spin-orbit torque at the Ir/Co interface, Phys. Rev. B 99, 134421 (2019).
- [25] S.-W. C. Shuai Dong, J.-M. Liu, and Z. Ren, Multiferroic materials and magnetoelectric physics: Symmetry, entanglement, excitation, and topology, Adv. Phys. **64**, 519 (2015).

- [26] Y. Takeuchi, Y. Yamane, J.-Y. Yoon, R. Itoh, B. Jinnai, S. Kanai, J. Ieda, S. Fukami, and H. Ohno, Chiral-spin rotation of noncollinear antiferromagnet by spin-orbit torque, Nat. Mater. 20, 1364 (2021).
- [27] I. Dzyaloshinsky, A thermodynamic theory of "weak" ferromagnetism of antiferromagnetics, J. Phys. Chem. Solids **4**, 241 (1958).
- [28] T. Moriya, Anisotropic superexchange interaction and weak ferromagnetism, Phys. Rev. **120**, 91 (1960).
- [29] H. Yang, J. Liang, and Q. Cui, First-principles calculations for Dzyaloshinskii-Moriya interaction, Nat. Rev. Phys. **5**, 43 (2023).
- [30] H. J. Zhao, P. Chen, S. Prosandeev, S. Artyukhin, and L. Bellaiche, Dzyaloshinskii–Moriya-like interaction in ferroelectrics and antiferroelectrics, Nat. Mater. 20, 341 (2021).
- [31] H. Katsura, N. Nagaosa, and A. V. Balatsky, Spin current and magnetoelectric effect in noncollinear magnets, Phys. Rev. Lett. 95, 057205 (2005).
- [32] D. Rusu, J. J. Peters, T. P. Hase, J. A. Gott, G. A. Nisbet, J. Strempfer, D. Haskel, S. D. Seddon, R. Beanland, A. M. Sanchez *et al.*, Ferroelectric incommensurate spin crystals, Nature (London) 602, 240 (2022).
- [33] P. Chen, H. J. Zhao, S. Prosandeev, S. Artyukhin, and L. Bellaiche, Microscopic origin of the electric Dzyaloshinskii-Moriya interaction, Phys. Rev. B 106, 224101 (2022).
- [34] D. Cassi, Phase transitions and random walks on graphs: A generalization of the Mermin-Wagner theorem to disordered lattices, fractals, and other discrete structures, Phys. Rev. Lett. **68**, 3631 (1992).
- [35] N. D. Mermin and H. Wagner, Absence of ferromagnetism or antiferromagnetism in one- or two-dimensional isotropic Heisenberg models, Phys. Rev. Lett. 17, 1133 (1966).
- [36] C. Dai, V. A. Stoica, S. Das, Z. Hong, L. W. Martin, R. Ramesh, J. W. Freeland, H. Wen, V. Gopalan, and L.-Q. Chen, Tunable nanoscale evolution and topological phase transitions of a polar vortex supercrystal, Adv. Mater. 34, 2106401 (2022).
- [37] A. Fernandez, M. Acharya, H.-G. Lee, J. Schimpf, Y. Jiang, D. Lou, Z. Tian, and L. W. Martin, Thin-film ferroelectrics, Adv. Mater. 34, 2108841 (2022).
- [38] F. Ferrari, S. Niu, J. Hasik, Y. Iqbal, D. Poilblanc, and F. Becca, Static and dynamical signatures of Dzyaloshinskii-Moriya interactions in the Heisenberg model on the Kagome lattice, SciPost Phys. 14, 139 (2023).
- [39] See Supplemental Material at http://link.aps.org/supplemental/ 10.1103/h6j7-cgwz for further technical details supporting the findings in the main text.
- [40] P. Villegas, T. Gili, G. Caldarelli, and A. Gabrielli, Laplacian renormalization group for heterogeneous networks, Nat. Phys. 19, 445 (2023).
- [41] P. Villegas, A. Gabrielli, F. Santucci, G. Caldarelli, and T. Gili, Laplacian paths in complex networks: Information core emerges from entropic transitions, Phys. Rev. Res. 4, 033196 (2022)
- [42] A. Poggialini, P. Villegas, M. A. Muñoz, and A. Gabrielli, Networks with many structural scales: A renormalization group perspective, Phys. Rev. Lett. 134, 057401 (2025).
- [43] A. Ortiz-Ambriz, C. Nisoli, C. Reichhardt, C. J. O. Reichhardt, and P. Tierno, Colloquium: Ice rule and emergent frustration in particle ice and beyond, Rev. Mod. Phys. 91, 041003 (2019).

- [44] P. Villegas, J. Hidalgo, P. Moretti, and M. A. Muñoz, Complex synchronization patterns in the human connectome network, in *Proceedings of ECCS 2014*, Springer Proceedings in Complexity, edited by S. Battiston, F. De Pellegrini, G. Caldarelli, and E. Merelli (Springer, Cham, 2016), pp. 69–80.
- [45] P. Moretti and M. Muñoz, Griffiths phases and the stretching of criticality in brain networks, Nat. Commun. 4, 2521 (2013).
- [46] D. Pierangeli, A. Tavani, F. Di Mei, A. J. Agranat, C. Conti, and E. DelRe, Observation of replica symmetry breaking in disordered nonlinear wave propagation, Nat. Commun. 8, 1501 (2017).
- [47] C. Li, X. Wang, Y. Wu, F. Liang, F. Wang, X. Zhao, H. Yu, and H. Zhang, Three-dimensional nonlinear photonic crystal in naturally grown potassium–tantalate–niobate perovskite ferroelectrics, Light Sci. Appl. 9, 193 (2020).
- [48] Y. Wu, X. Wang, G. Tian, L. Zheng, F. Liang, S. Zhang, H. Yu, and H. Zhang, Inverse design of ferroelectric-order in per-ovskite crystal for self-powered ultraviolet photodetection, Adv. Mater. 34, 2105108 (2022).
- [49] Y. Wu, Q. Liu, G. Tian, L. Zheng, F. Liang, X. Wang, D. Wang, Y. Sang, H. Liu, J. Wang *et al.*, Periodically poled nonlinear photonic crystal KTa_{0.51}Nb_{0.49}O₃ combining wide transparent range and large quadratic coefficient, Adv. Opt. Mater. 10, 2201010 (2022).
- [50] Y.-C. Chang, C. Wang, S. Yin, R. C. Hoffman, and A. G. Mott, Giant electro-optic effect in nanodisordered KTN crystals, Opt. Lett. 38, 4574 (2013).
- [51] B. Noheda, D. Cox, G. Shirane, J. Gonzalo, L. Cross, and S. Park, A monoclinic ferroelectric phase in the Pb(Zr1- xTix)O₃ solid solution, Appl. Phys. Lett. 74, 2059 (1999).
- [52] V. V. Shvartsman and D. C. Lupascu, Lead-free relaxor ferroelectrics, J. Am. Ceram. Soc. 95, 1 (2012).
- [53] F. Di Mei, L. Falsi, M. Flammini, D. Pierangeli, P. Di Porto, A. Agranat, and E. DelRe, Giant broadband refraction in the visible in a ferroelectric perovskite, Nat. Photonics 12, 734 (2018).
- [54] L. Falsi, L. Tartara, F. Di Mei, M. Flammini, J. Parravicini, D. Pierangeli, G. Parravicini, F. Xin, P. DiPorto, A. J. Agranat et al., Constraint-free wavelength conversion supported by giant optical refraction in a 3D perovskite supercrystal, Commun. Mater. 1, 76 (2020).
- [55] L. Falsi, S. Macis, Y. Gelkop, L. Tartara, E. Bonaventura, P. Di Pietro, A. Perucchi, Y. Garcia, G. Perepelitsa, E. DelRe et al., Anomalous optical properties of KTN:Li ferroelectric supercrystals, Nanomaterials 13, 899 (2023).
- [56] L. Falsi, M. Aversa, F. Di Mei, D. Pierangeli, F. Xin, A. J. Agranat, and E. DelRe, Direct observation of fractaldimensional percolation in the 3D cluster dynamics of a ferroelectric supercrystal, Phys. Rev. Lett. 126, 037601 (2021).
- [57] M. Ferraro, D. Pierangeli, M. Flammini, G. Di Domenico, L. Falsi, F. Di Mei, A. Agranat, and E. DelRe, Observation of polarization-maintaining light propagation in depoled compositionally disordered ferroelectrics, Opt. Lett. 42, 3856 (2017).
- [58] F. Colaiori, Exactly solvable model of avalanches dynamics for Barkhausen crackling noise, Adv. Phys. **57**, 287 (2008).
- [59] M. F. Atiyah, *The Geometry and Physics of Knots* (Cambridge University Press, Cambridge, 1990).
- [60] L. H. Kauffman, Knots and Physics (World Scientific, Singapore, 2001), Vol. 1.

- [61] D. Rolfsen, Knots and Links (American Mathematical Society, Berkeley, CA, 2003), Vol. 346.
- [62] J. C. Turner, P. Van De Griend, and C. Warner, History and Science of Knots (World Scientific, Singapore, 1996), Vol. 11.
- [63] L. Faddeev and A. J. Niemi, Stable knot-like structures in classical field theory, Nature (London) **387**, 58 (1997).
- [64] U. Tkalec, M. Ravnik, S. Čopar, S. Žumer, and I. Muševič, Reconfigurable knots and links in chiral nematic colloids, Science 333, 62 (2011).
- [65] D. Kleckner and W. T. Irvine, Creation and dynamics of knotted vortices, Nat. Phys. 9, 253 (2013).
- [66] P. Sutcliffe, Skyrmion knots in frustrated magnets, Phys. Rev. Lett. 118, 247203 (2017).
- [67] F. Zheng, N. S. Kiselev, F. N. Rybakov, L. Yang, W. Shi, S. Blügel, and R. E. Dunin-Borkowski, Hopfion rings in a cubic chiral magnet, Nature (London) 623, 718 (2023).
- [68] K.-E. Kim, S. Jeong, K. Chu, J. H. Lee, G.-Y. Kim, F. Xue, T. Y. Koo, L.-Q. Chen, S.-Y. Choi, R. Ramesh *et al.*, Configurable topological textures in strain graded ferroelectric nanoplates, Nat. Commun. 9, 403 (2018).
- [69] Y. Tang, Y. Zhu, X. Ma, A. Y. Borisevich, A. N. Morozovska, E. A. Eliseev, W. Wang, Y. Wang, Y. Xu, Z. Zhang *et al.*, Observation of a periodic array of flux-closure quadrants in strained ferroelectric PbTiO₃ films, Science **348**, 547 (2015).
- [70] X. Li, C. Tan, C. Liu, P. Gao, Y. Sun, P. Chen, M. Li, L. Liao, R. Zhu, J. Wang *et al.*, Atomic-scale observations of electrical and mechanical manipulation of topological polar flux closure, Proc. Natl. Acad. Sci. USA 117, 18954 (2020).
- [71] J. Seidel, R. K. Vasudevan, and N. Valanoor, Topological structures in multiferroics—domain walls, skyrmions and vortices, Adv. Electron. Mater. **2**, 1500292 (2016).
- [72] I. I. Naumov, L. Bellaiche, and H. Fu, Unusual phase transitions in ferroelectric nanodisks and nanorods, Nature (London) 432, 737 (2004).
- [73] A. Fert, V. Cros, and J. Sampaio, Skyrmions on the track, Nat. Nanotechnol. 8, 152 (2013).
- [74] J. Scott, Multiferroic memories, Nat. Mater. 6, 256 (2007).
- [75] H. Du, X. Zhao, F. N. Rybakov, A. B. Borisov, S. Wang, J. Tang, C. Jin, C. Wang, W. Wei, N. S. Kiselev, Y. Zhang, R. Che, S. Blügel, and M. Tian, Interaction of individual skyrmions in a nanostructured cubic chiral magnet, Phys. Rev. Lett. 120, 197203 (2018).
- [76] J. Wild, T. N. Meier, S. Pöllath, M. Kronseder, A. Bauer, A. Chacon, M. Halder, M. Schowalter, A. Rosenauer, J. Zweck et al., Entropy-limited topological protection of skyrmions, Sci. Adv. 3, e1701704 (2017).

- [77] Y. Nahas, S. Prokhorenko, I. Kornev, and L. Bellaiche, Topological point defects in relaxor ferroelectrics, Phys. Rev. Lett. 116, 127601 (2016).
- [78] D. J. Amit, H. Gutfreund, and H. Sompolinsky, Spin-glass models of neural networks, Phys. Rev. A 32, 1007 (1985).
- [79] R. A. Goldstein, Z. A. Luthey-Schulten, and P. G. Wolynes, Optimal protein-folding codes from spin-glass theory, Proc. Natl. Acad. Sci. USA 89, 4918 (1992).
- [80] P. Villegas, P. Moretti, and M. A. Muñoz, Frustrated hierarchical synchronization and emergent complexity in the human connectome network, Sci. Rep. 4, 5990 (2014).
- [81] T. Itou, E. Watanabe, S. Maegawa, A. Tajima, N. Tajima, K. Kubo, R. Kato, and K. Kanoda, Slow dynamics of electrons at a metal-Mott insulator boundary in an organic system with disorder, Sci. Adv. 3, e1601594 (2017).
- [82] L. E. Cross, Relaxorferroelectrics: An overview, Ferroelectrics 151, 305 (1994).
- [83] G. Burns and F. Dacol, Crystalline ferroelectrics with glassy polarization behavior, Phys. Rev. B 28, 2527 (1983).
- [84] P. Timonin, Griffiths' phase in dilute ferroelectrics, Ferroelectrics **199**, 69 (1997).
- [85] D. Sherrington, Relaxors, spin, stoner and cluster glasses, Phase Transitions 88, 202 (2015).
- [86] H. Zheng, T. Zhou, D. Sheyfer, J. Kim, J. Kim, T. D. Frazer, Z. Cai, M. V. Holt, Z. Zhang, J. Mitchell *et al.*, Heterogeneous field response of hierarchical polar laminates in relaxor ferroelectrics, Science 384, 1447 (2024).
- [87] S. Prosandeev, D. Wang, A. R. Akbarzadeh, B. Dkhil, and L. Bellaiche, Field-induced percolation of polar nanoregions in relaxor ferroelectrics, Phys. Rev. Lett. 110, 207601 (2013).
- [88] A. L. Goodwin, Opportunities and challenges in understanding complex functional materials, Nat. Commun. 10, 4461 (2019).
- [89] G. Nataf, M. Guennou, J. Gregg, D. Meier, J. Hlinka, E. Salje, and J. Kreisel, Domain-wall engineering and topological defects in ferroelectric and ferroelastic materials, Nat. Rev. Phys. 2, 634 (2020).
- [90] R. De Vogli, J. Montomoli, G. Abu-Sittah, and I. Pappé, Break the selective silence on the genocide in Gaza, The Lancet 406, 688 (2025).
- [91] L. Lo Presti, J. Parravicini, R. Soave, G. Parravicini, M. Mauri, L. Loconte, F. Di Mei, L. Falsi, L. Tartara, S. Binetti, A. J. Agranat, and E. DelRe, Observation of an exotic lattice structure in the transparent KTa_{1-x}Nb_xO₃ perovskite supercrystal, Phys. Rev. B 102, 214110 (2020).